Background subtraction for open heavy flavour studies in proton-proton collisions at $\sqrt{s} = 7$ TeV with the ALICE Muon Spectrometer

Fatiha Lehas

UFR sciences et technologies

Laboratoire de physique corpusculaire

Blaise Pascal University

Master Report

Background subtraction for open heavy flavour studies in proton-proton collisions at $\sqrt{s} = 7$ TeV with the ALICE Muon Spectrometer

Author:
Fatiha LEHAS

Supervisor:
Dr. Lizardo Valencia Palomo

June 2014

Abstract

With ultrarelativistic high energy heavy-ion collisions it is possible to reproduce, during a short time, the Quark Gluon Plasma : a dense and hot matter that existed in the early universe some microseconds after the big bang. Among the experiments at the LHC, ALICE is the only one that was designed and built to study heavy ion collisions. The muon spectrometer of the ALICE experiment studies open heavy flavours, quarkonium and low mass resonance through their semileptonic and leptonic decay into single muons and dimuons. The present report focuses on the study of open heavy flavours in proton-proton collisions as they can be used to test perturbative QCD calculations but also as a reference in Pb-Pb collision measurements. The first chapter introduces basic concepts of heavy ion collisions and open heavy flavour production in proton proton collisions. The second chapter contains a description of the ALICE experiment and the muon spectrometer. Chapter three describes the method used to extract the single muon distribution coming from open heavy flavours and the associated systematic uncertainties to the background subtraction. Finally, chapter four is a summary of the most important results obtained.

Résumé

Avec les collisions des ions lourds à des energies ultrarelativistes il est possible de reproduire, pendant un court lap de temps, une plasma de quark et de gluon (QGP) : une matière dense et chaude qui existait dans l'univers primordial quelques microsecondes aprés le big bang. Parmi les expériences au LHC, ALICE est la seule qui a été conçu et construite pour étudier les collisions d'ions lourds. Le spectromètre à muons de l'expérience ALICE étudie les saveurs lourdes ouvertes, quarkonium et les résonances à faible masse à travers leurs désintégration leptonique et semileptonique en muons et dimuons. Le rapport actuel se concentre sur l'étude des saveurs lourdes ouvertes dans les collisions proton-proton comme ils peuvent être utilisés pour tester les calculs de la QCD perturbative mais aussi comme une référence dans les collisions Pb-Pb. Le premier chapitre introduit les concepts basiques des collisions des ions lourdes et la production des saveurs lourdes ouvertes dans les collisions protons-protons. Le deuxième chapitre contient une description de l'expérience ALICE et le spectromètre à muons. Le chapitre trois décrit la méthode utilisée pour extraire la distribution du muon provenant des saveurs lourdes ouvertes et les uncertitudes systématiques associées à la soustraction du bruit de fonds. Finalement, le chapitre quatre est un résumé des résultats les plus importants obtenus.

Acknowledgements

I thank Allah the Almighty for giving me the will and courage to complete this modest master's report. I extend my thanks to my project advisor, Doctor.Lizardo Valencia Palomo, for his invaluable advice and availability throughout the preparation of this work. I am thankful to the ALICE group in the LPC at Clermont-Ferrand for their collaboration. I want to thank all my friends who helped me from far and near to complete this work. I conclude by thanking my parents that I have always trusted.

Contents

Abstract ii

Résumé iii

Acknowledgements iv

Contents v

List of Figures vii

List of Tables ix

1 Introduction 1
- 1.1 Preleminaries . . . 1
- 1.2 QCD phase transition diagram . . . 2
- 1.3 Nucleus-nucleus collisions . . . 3
  - 1.3.1 Space-time evolution . . . 4
  - 1.3.2 The importance of open heavy flavours . . . 5
  - 1.3.3 Factorization theorem . . . 6
  - 1.3.4 Open heavy flavour in pp collision . . . 7

2 ALICE Experiment 9
- 2.1 The Large Hadron Collider . . . 9
- 2.2 The ALICE Experiment . . . 11
  - 2.2.1 Central barrel . . . 11
  - 2.2.2 Forward Muon spectrometer . . . 14
  - 2.2.3 Absorbers . . . 15
  - 2.2.4 Tracking system . . . 15
  - 2.2.5 Trigger system . . . 16
  - 2.2.6 Dipole magnet . . . 16

3 Background subtraction 17
- 3.1 Realistic simulations . . . 17
- 3.2 p_T-shape of the background . . . 19
- 3.3 Background Normalization . . . 22
- 3.4 Results . . . 24
- 3.5 Systematic uncertainties . . . 25

4 Conclusion **29**

A π/K Dominant Primary particles **31**

B Scaling factors **35**

Bibliography **37**

List of Figures

1.1 QCD phase diagram. 2
1.2 The time evolution of the collision of two nuclei. 4

2.1 Layout of the acceleration chain at CERN 10
2.2 The ALICE experiment 12
2.3 The forward Muon spectrometer layout of main components. An absorber to filter the background, a set of tracking chambers before, inside and after the magnet and a set of trigger chambers. 14

3.1 Transverse momentum ditributions of muon track sources in pp collisions at $\sqrt{s} = 7$ TeV obtained from simulations with PYTHIA, without (left) and with (right) event and track selection. 17
3.2 The production mechanisms for different muon track sources. 18
3.3 Fit and extrapolation of the primary muons p_t-spectrum in the 5η bins using PYTHIA (left) and PhoJet (right). 20
3.4 Comparison between the p_T-shape of primary muons in the total accepatnce $-4.0 < \eta < -2.5$ (red line) and the sum from the fit in the 5 pseudo-rapidity bins (green lines). Left panel : PYTHIA. Right panel : PhoJet. . 21
3.5 Estimated ratio of primaries (scaled) to inclusive muons for real data and Monte Carlo simulations (left) and comparison between the inclusive spectrums of real data and Monte Carlo simulations (right) in the 5 η bins. 23
3.6 The same as figure.3.5 in $-4.0 < \eta < -2.5$. 24
3.7 Left panel : yield of muons before background subtraction and the mean yield after the background subtraction from PYTHIA and PhoJet as a function of p_T in $-4.0 < \eta < -2.5$. Right panel : yield of muons before and after background subtraction as a function of η and for $2 < p_T < 20$ GeV. 25
3.8 Estimated systematic uncertainties for σ_{model} (left) and σ_{norm} (right) in the 5 η bins. 26
3.9 Estimated systematic uncertainties for σ_{model} (left) and σ_{norm} (right) in the total acceptance. 27

List of Tables

3.1 Estimated systematic uncertainties for σ_{model} and σ_{norm}. 28

A.1 Produced primary particles according to PYTHIA 31
A.2 Produced open charm particles according to PYTHIA 32
A.3 Produced open beauty particles according to PYTHIA 32
A.4 Produced primary particles according to PhoJet 32
A.5 Produced open charm particles according to PhoJet 32
A.6 Produced open beauty particles according to PhoJet 33

B.1 Scaling factors (rounded) used to scale the background to the real data . 35
B.2 Scaling factors used for background subtraction and to compute σ_{norm}. . 36

Chapter 1

Introduction

In this chapter, we present the importance of heavy ion collisions studies and how it is related to the Quark-Gluon-Plasma. Production of open heavy flavour in proton-proton collision and their role to verify pertubative QCD calculations are also presented.

1.1 Preleminaries

The heavy flavour discovery took place in 1974 when the J/ψ particle was first registered. The particle was identified as a bound state of the quark charm and its anti-quark. It was not only the discovery of a new particle but also the discovery of a fourth quark after the u, d and s. Other heavy particles, which one of the constituants was a c quark, are called open charm like Λ_c^+, D^0 and D^+ that were discovered in 1975 and 1976 repectively. In 1977, the Υ particle, a bound state of beauty (bottom) quark and its anti-quark, was discovered. Five years later, the open beauty particles B^0 and B^+ were discovered [1].

The production of heavy flavours can only occur in the initial hard scatterings of the collision because of their large mass. It is then possible to use perturbative QCD (pQCD) calculations to compute heavy flavours production cross-sections. Besides that, the charm and beauty hadrons became a powerful tool to investigate the properties of the dense and hot medium that is created in ultra-relativistic heavy ion collisions.

At the present LHC energies, 2.75 TeV for Pb-Pb collisions, charm and beauty production is abundant: the cross-section increases by about a factor 10 for charm and 100 for beauty with respect to RHIC top energy. The large yields of c and b quarks allow detailed studies on the heavy flavour energy loss as well as on the possible charm and

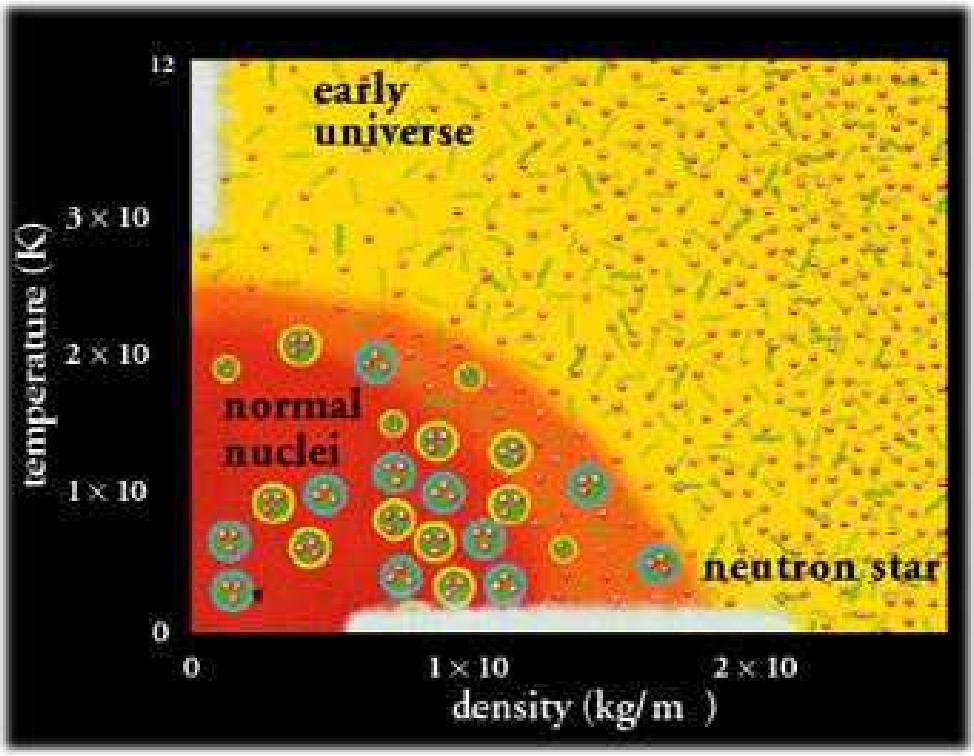

FIGURE 1.1: QCD phase diagram.

beauty thermalization in the QCD medium. On this respect, in order to constrain theoretical models, it is of crucial importance to have an experimental apparatus capable of measuring separately open charm and beauty hadrons [2].

1.2 QCD phase transition diagram

Lattice QCD calculations predict that at sufficiently high energy density and temperature, ordinary nuclear matter undergoes a phase transition from a confined to a deconfined state where quarks and gluons are asymptotically free. This new state of matter is called Quark-Gluon-Plasma (QGP) (figure.1.1) and is thought to have existed in the early universe some microseconds after the big bang. The only way to recreate the QGP in the laboratory is by reproducing the same conditions of high energy density and temperature with high energy heavy-ion collisions.

The basic idea in heavy ion collisions, is that a large amount of energy is deposited in a small volume [3, 4].

A considerable attention has been paid to whether a critical point exists on the phase diagram of strongly interacting matter. One very important issue is whether the critical point can be found in experiments that involve colliding heavy nuclei.

The QCD phase diagram has two axes: the temperature T and the density (chemical potential for quark number) μ. The chemical potential is directly related to the net quark density (i.e., the number of quark minus number of antiquarks). We can extract the main features of the QCD phase diagram by first setting either μ or T to zero. Imagine the early universe when its temperature was much higher than the critical temperature of deconfinement, which is about 200 MeV. The early universe contained practically the same number of quarks and antiquarks, (so $\mu = 0$.) At such high temperatures, we have a plasma of quarks and gluons, and the interaction between these particles is weak, thanks to asymptotic freedom.

As the universe cools down, the interaction becomes stronger and two things happen. The first is confinement: quarks and gluons are combined into hadrons (bound states of three quarks, or one quark and one antiquark). There does not have to be a phase transition associated with confinement alone (in a later state in the evolution of the universe, electrons and protons would recombine into hydrogen without going through phase transition).

The second phenomenon is spontaneous breaking of chiral symmetry. Under chiral symmetry, different types of left handed quarks (with spin pointing against the direction of motion) transform into each other (right to left handed and left to right handed), while independently right-handed quarks (spin pointing to the same direction as momentum) transform into each other. Chiral symmetry would be an exact symmetry of QCD if quarks were massless. In the real world u and d quark (i.e., the two types of quarks that combine to form neutrons and protons) are not massless, but very light, so the chiral symmetry is not exact.

Let us now stay on the other axis, at zero temperature, by increasing the quark chemical potential (see figure.1.1), one first jumps from vacuum to nuclear matter. This jump is definitely a first-order phase transition and what happens at higher chemical potential is less clear. It is rather well established that if u and d are the only relevant quarks, then at extremely high densities chiral symmetry should be restored. Therefore, there must be another chiral phase transition on the μ axis. In contrast to the finite-temperature chiral phase transition, there is no reliable information about the location and the nature of this chiral phase transition [4].

1.3 Nucleus-nucleus collisions

The principle purpose of ultrarelativistic nucleus-nucleus collisions is to obtain information on the QCD phase diagram. Indeed, it was argued that the quark-hadron phase

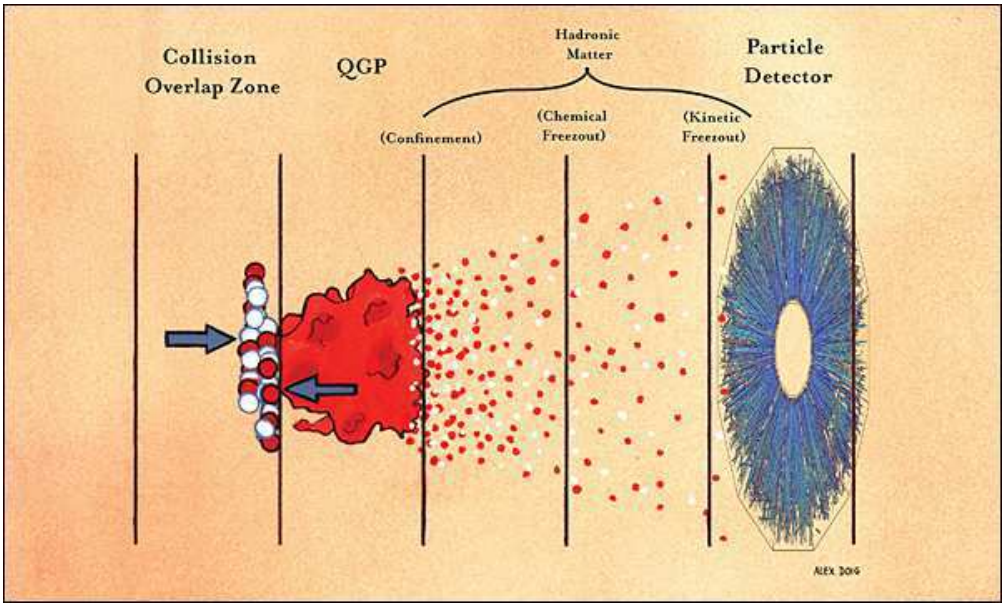

FIGURE 1.2: The time evolution of the collision of two nuclei.

transition drives the equilibration dynamically, at least for the SPS energies and above [5].

During the process of multiple nucleon-nucleon collision occurring in a nucleus-nucleus collisions, the nucleons lose a fraction of their energy. At low energies, nucleons are stopped in the collision region, giving birth to a state with high chemical potential μ_B. At very high energies, the nucleons can still have enough momentum to continue with their trajectory and move far away from the interaction point. The energy lost is then deposited in the collision region creating a high energy nuclear matter with small μ_B.

1.3.1 Space-time evolution

If the energy of the collision is high enough, the QGP can be created. If the plasma reaches the thermal equilibrium, its evolution will follow the laws of thermodynamics. As the system expands, its temperature also drops down, giving place to hadronization. The space-time evolution of a high energy heavy-ion collision is the following (see figure.1.2) [3, 6].

- Heavy quarks, jets and direct photons are created in the initial hard scattering (t $\approx$ 0 fm/c). These processes are well described by pQCD.
- Multiple scattering among partons and produced particles lead to a rapid increase of entropy which could result in thermalization (t $\approx$ 1-2 fm/c).
- The system reaches the deconfined phase (t $\approx$ 10-15 fm/c).

- The expanding system cools down and below the critical temperature quarks and gluons become confined into hadrons (t $\approx$ 20 fm/c).
- Inelastic processes are reduced until the relative abundance of hadrons is fixed (chemical freeze-out). Finally, all the interactions cease and created hadrons stream out (kinetic freeze-out).

The standard scenario for a high energy nucleus-nucleus collision involves several stages (see figure.1.2). At extremely short times scales take place the very hard processes that account for the hard particles in the final state. The bulk of this particle production takes place slightly later (t $\sim$ 0.2 fm/c). Eventually, this deconfined matter reaches a state of local thermal equilibrium, and can be described by hydrodynamics. Because it is in expansion, it cools down and reaches the critical temperature where hadrons are formed again. At a later stage, the density becomes too low to have an interaction rate high enough to sustain equilibrium, and the system freezes out.

Experimentally, one is trying to infer properties of the early and intermediate stages of these collisions from the measured hadrons in the final state [3].

1.3.2 The importance of open heavy flavours

With the new scale of energy in Pb-Pb collision at the LHC, ten times higher than that reached by Relativitic Heavy Ion Collider (RHIC), a deconfined state of quarks and gluons is expected to be formed ($\mu_B \approx 0$). Since the lifetime of that medium ($\approx$ 0.5 - 1 fm/c) is larger than the production time scale of the heavy flavours ($1/m_Q$), then heavy quarks play a crucial role to study the properties and provide information on that new state of matter [7].

Heavy quarks can be used as probes to understand the in-medium partonic energy loss in the dense QCD matter created in a central heavy-ion collision.

The nuclear modification factor R_{AA} is an experimental observable defined by the equation.1.1. It quantifies the deviation of particle production in nucleus-nucleus collisions with respect to proton collisions binary scaling.

$$R_{AA} = \frac{1}{< N_{coll} >} \times \frac{d^2N_{AA}/dp_t d\eta}{d^2N_{pp}/dp_t d\eta} \tag{1.1}$$

where $d^2N_{AA}/dp_t d\eta$ is the number of measured particles per unit of transverse momentum and pseudorapidity in A-A collisions, $d^2N_{pp}/dp_t d\eta$ the number of the same kind of particles measured in pp collisios and $< N_{coll} >$ the mean number of nucleon-nucleon

collisions. If $R_{AA} = 1$, then there is no difference between the production in nucleus-nucleus and in pp collisions. But if $R_{AA} \neq 1$, then it might be an indication of medium induced effects [2, 8].

Measurements of the heavy-flavour production in proton-proton collisions are necessary to obtain the nuclear modification factor. Moreover, studies of charm and beauty production in pp collisions at the LHC allows to test pQCD models in a new energy domain [9].

1.3.3 Factorization theorem

The theoretical predictions in nucleon-nucleon collisions are based on the factorization theorem in the framework of the pQCD calculations to compute the cross section for heavy flavours.

According to that theorem, the process of nucleon-nucleon collisions could be explained in the following steps:

- In the initial stage, two partons i and j are extracted from the two colliding nucleon each of momentum $x_{i/j}$ with probablities given by the parton distribution function $f_{i/j}(x_{i/j}, \mu_F^2)$ such that i/j is parton species (q,$\bar{q}$,g) and μ_F is the factorization scale.
- In the following stage and during hard scatterings between the two partons, heavy flavours are produced with virtuality $Q \sim x_1 x_2 S_{NN}$ where S_{NN} is the center of mass energy. In that stage, when $m_Q > \Lambda_{QCD}$, the elementary cross section is related to the interaction at high Q^2 and can be computed in pQCD in terms of α_s^k. α_s is the strong coupling constant and k indicates the perturbative order.
- After the formation of the heavy quark, it will interact with other partons and hadronize into open heavy flavour hadrons with a probability $D_Q^{H_Q}(z)$ where z is the momentum fraction p^{H_Q}/p^Q.

So according to those three steps, the hadronic production of open heavy flavours is characterized by three quantities: $f_{i/j}(x, \mu_F)$ partonic distribution function (PDFs), partonic cross section $d\hat{\sigma}^{ij\to Q(\bar{Q})n}/d\hat{p}_t$ and the fragmentation function $D_Q^{H_Q}(z)$. The large mass of open heavy flavour hadrons makes those three parameters different in properties than light hadrons.

One of the advantages of heavy flavours is that they allow to access small Bjorken-x range, in particular at high center-of-mass collision energy and/or large (pseudo)-rapidity. At LHC energies, in pp collisions at $\sqrt{s_{NN}} = 7$ TeV, one can access Bjorken-x

values down to $x \sim 4.10^{-4}$ (1.10^{-3}) for charm (beauty) quarks in the mid-rapidity region. Thanks to higher energies reached at the LHC than at RHIC, heavy quarks allow to probe the low Bjorken-x region dominated by gluons at the LHC. When the rapidity increases, unprecedented low Bjorken-x values can be investigated. In the acceptance of the forward muon spectrometer of ALICE, $-4.0 < \eta < -2.5$, the accessible Bjorken-x range is down to 10^{-6}.

In the partonic cross section, each order of α_s is accompanied by logarithmic terms as a coefficient $\sim (\alpha_s ln\tau)^n$ (τ is an arbitrary order parameter) when the perturbative series end up. A Fix Order (FO, with a given power n) cross section is used to different orders of logarithmic terms.

For $n = 0$, one obtains the Leading Order (LO) cross section with $\mathcal{O}(\alpha_s)$(or the Born term) and $n = 1$ ($\mathcal{O}(\alpha_s^2)$) corresponds to the Next-to-Leading Order (NLO) cross section. With a given fixed order n and using $k = n$ one obtains the Leading Logarithm (LL) terms. The Next-to-Leading Logarithm (NLL) terms are obtained by adding to the LL terms the $k = n - 1$ terms. For reasonable consideration FO and NLL calculations were matched as the so called FONLL (Fixed-Order Next-to-Leading Logarithm) formalism.

1.3.4 Open heavy flavour in pp collision

The production cross section of b and c quarks can be predicted using pQCD due to their large masses ($m_Q > \Lambda_{QCD}$). The predictions by the different models do not give the complete description of non perturbative phenomena that contribute in heavy flavour production.

Heavy flavours studies were performed by different experiments at Tevatron and RHIC. D meson production cross section was measured at $\sqrt{s} = 1.96$ TeV and compared to FONLL calculations. The measured differential cross sections was found to be higher than the theoretical predictions by about 100% at low p_t and 50% at high p_t, but they are compatible with the calculations within uncertainty bands.

In the case of beauty quark, the measurements were different. The production cross section were better described by theory. The J/ψ p_t distribution from the inclusive decays $B \to J/\psi + X$ was measured by the CDF collaboration. It was found that the data points lie well within the uncertainty band and they are in very good agreement with the central FONLL prediction [1, 10–12].

Chapter 2

ALICE Experiment

In the following chapter we will present the Large Hadron collider (LHC) and the principle experiments that take part in it. Then, we will talk about the ALICE experiment and its components. Finally, we explain in more detail the forward muon spectrometer which was the detector used for this report.

2.1 The Large Hadron Collider

The Large Hadron Collider (LHC) is the world's largest and most powerful particle accelerator designed for particle physics research. It was built by CERN from 1998 to 2008 and started up in November 2009. It is designed to collide proton beams at a center of mass energy of 14 TeV but it can also collide heavy ions at a center of mass energy of 5.5 TeV per nucleon pair.

The journey of particles in the largest and most powerful accelerator engine begins with a gas cylinder from which hydrogen atoms flow in controlled rate into a source chamber of a linear accelerator (LINAC 2) where electrons are removed to leave hydrogen nuclei that are in turn accelerated by an electric field. In the LINAC 2, the packet of protons are accelerated up to 1/3 of the speed of light and are then sent to the Synchrotron Booster, the second stage of acceleration. The Booster is a 170 m in circumference accelerator. In order to accelerate the packets, they are repeatedly circulated and a pulsed electric field is applied. Magnets are also used to bend the beam of protons around the circle. The Booster accelerates the protons up to 90% of the speed of light and squeezes them. After that, the packet from the Booster flows to the Proton Synchrotron (PS) where it will begin the third stage of the acceleration. The Proton Synchrotron has 628 m in circumference and here the beam reaches 99.9% of the speed of light. The transition point is reached, a point where the energy added to the protons by the pulsating

electric field cannot translate into increasing velocity since they are already approaching the limit speed of light. The energy of each proton in Proton Synchrotron rises to 25 GeV where it is 25 times heavier than at rest. The packets of protons undergo the fourth stage of the acceleration in the Super Proton Synchrotron (SPS), 7 km in circumference that accelerates the protons, increasing their energy up to 450 GeV.

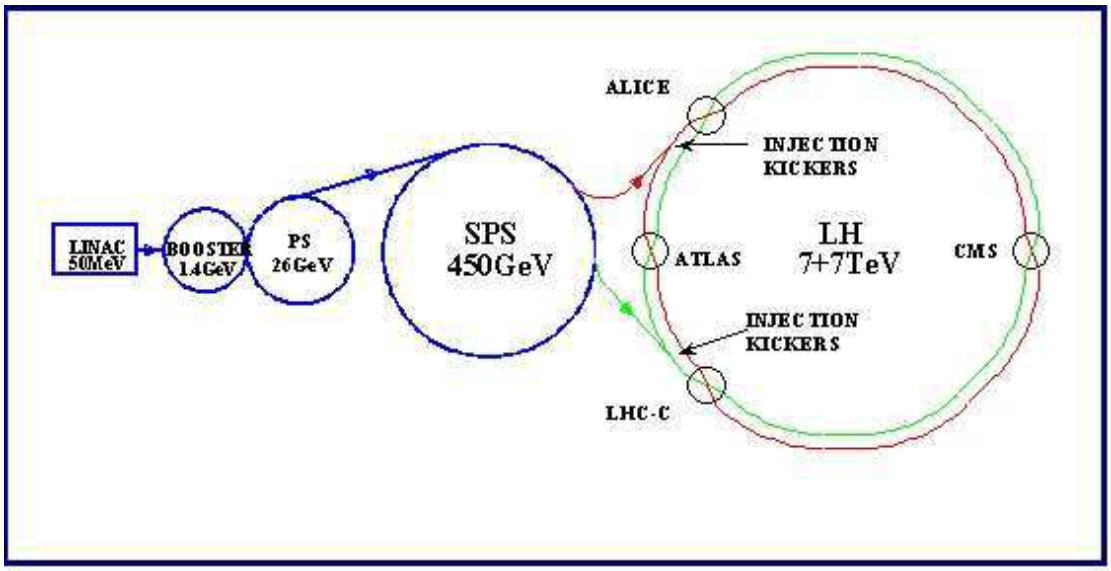

FIGURE 2.1: Layout of the acceleration chain at CERN

Finally, the packet of protons is transferred to the LHC. There are two vacuum pipes within the LHC containing proton beams travelling in opposite directions. The counter rotating beams crossover in the 4 detector caverns where they can collide [13, 14].

There are four main experiments at the LHC, each one located in each intersection point of the beams as it is shown in the figure.2.1. Each experiment is different and is characterized by its detectors [15];

- **ALICE** (A Large Ion Collider Experiment), the only experiment that was built and designed to study heavy ion collisions.

- **ATLAS** (A Toroidal LHC ApparatuS), its purpose is to search for the Higgs boson, particles that could make up dark matter and physics beyond the Standard Model.

- **CMS** (Compact Muon Solenoid), with similar objective as the ATLAS experiment.

- **LHCb** (Large Hadron Collider beauty), investigates the differences between matter and antimatter.

2.2 The ALICE Experiment

To reach their goals, the ALICE detector has been built using different technologies and instruments to manage the large multiplicities that characterize high energy heavy ion collisions.

The ALICE collaboration includes over 1000 physicists and engineers from 105 Institutes in 30 countries. Its overall dimensions are $16 \times 16 \times 26\ m^3$ with a total weight of approximately 10 000 ton [16].

We can mention two topics among many of the ALICE experiment physics program and that are related to heavy flavour mesurements :

- **Quarkonium** : study of the quarkonium states (Charmonium Ψ and Bottmonium Υ families) through the study of their spectrum as a function of p_t (to distangle QGP models), for different colliding nuclei (Pb-Pb or Ar-Ar, to investigate the dependence of quarkonia yields as a function of the system size), for p-p and p-nucleus (or d-nucleus or α-nucleus, to establish a reference for nucleus-nucleus).
- **Open Charm and Beauty** : represent a normalization of the quarkonia signals, in addition to that, the measurement of open heavy flavours may reveal mechanisms of heavy quarkonia others than direct hard-scattering. The study of the dimuon invariant mass spectrum gives an opportunity to study the production of open charm and beauty in parallel with the one of heavy quarkonia [17].

ALICE detector (figure.2.2) can be divided in two parts. The central barrel is placed inside a large solenoidal magnet (B=0.5 T) (to measure hadrons, electrons and photons) and the forward muon spectrometer (to measure dimuons and single muons).

2.2.1 Central barrel

The central barrel covers a polar angle from 45° to 135° and is embedded inside a large solenoid magnet. The elements that constitute the central barrel are the following :

- **Inner Tracking System** (ITS) consists of six layers of silicon pixel : the Silicon Pixel Dectecor (SPD), the Silicon Drift Detector (SDD) and the Silicon Strip Detector (SSD). The main task of the Inner Tracking System is to determine the primary and secondary vertices and Particle Identification. The ITS surrounds the beam pipe and is like a support for it as it avoids movement during the operation.

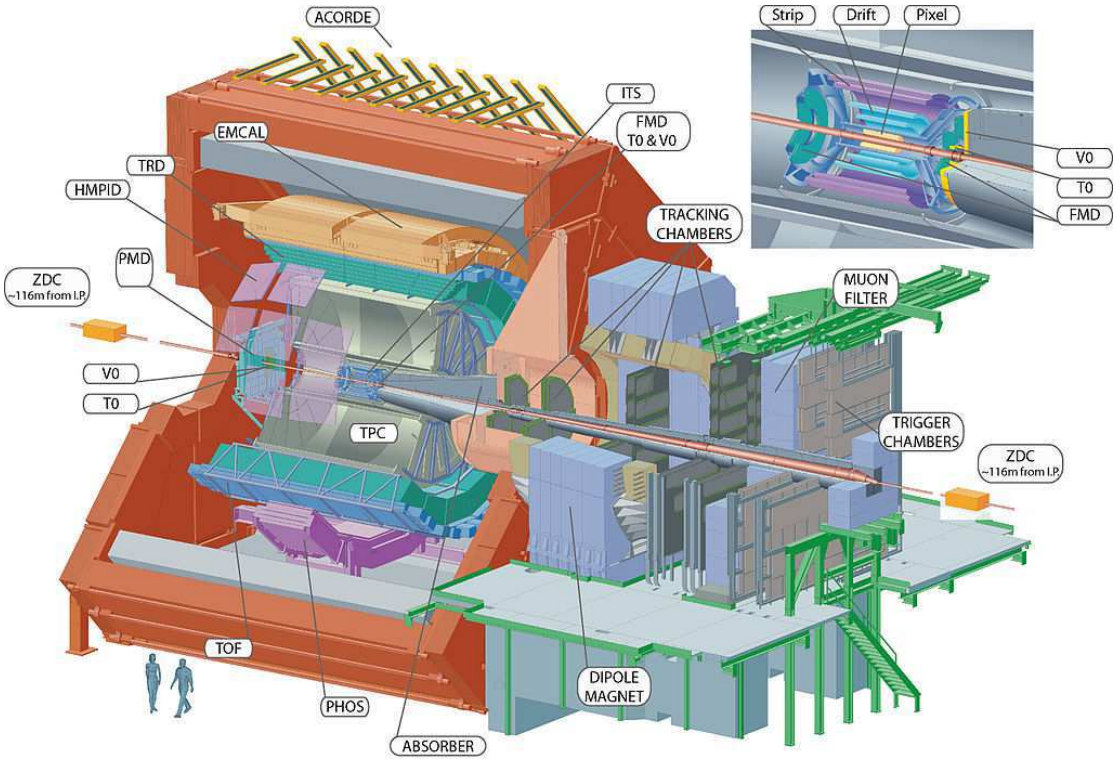

FIGURE 2.2: The ALICE experiment

The ITS system covers a common range of pseudorapidity $|\eta| < 0.9$. The elements that constitute the ITS are :

- The SPD is the two innermost layers of the ITS, its role is to provide adequate measurement of the primary and secondary vertex. It also measures the impact parameter of secondary tracks coming from the weak decay of strange, charm and beauty particles.

- The SDD is the two intermediate layers of the ITS. The SDD participates in particle identification by dE/dx technique and reconstructs secondary vertices.

- The SSD is the two outermost layers of the ITS. The SSD is used for matching tracks from TPC to the ITS and provides 2 dimensional measurement of the track position and also information on dE/dx which is used for particle identification [18].

- **Time-Projection Chamber** (TPC) is the main tracking device in the central barrel. The TPC performs the tracking and determines the momentum of charged particles. The range of pseudo-rapidity that the TPC covers is $|\eta| < 0.9$. The coverage range of the transverse momentum is from about 0.1 GeV/c to 100 GeV/c [19].

- **Time-Of-Flight** (TOF) has a modular structure that corresponds to 18 sectors in ϕ and it covers a cylindrical surface of polar acceptance $45° < \theta < 135°$ with

pseudorapidity range $|\eta| \lesssim 0.9$. The TOF measures the time that takes a particle to travel from the interaction vertex leading to the identification of the particles. Large samples of pions, kaons and protons are identified thanks to the coupling between the ITS, the TPC and the TOF [20].

- **High-Momentum Particle Idendification Detector** (HMPID) measures Cherenkov radiation (emitted radiation by charged particles at a speed greater than the velocity of light in the same medium). The aim is to enhance the PID capability of ALICE by enabling identification of charged hadrons beyond the momentum interval atteinable (above $p_t = 1$ GeV/c) through energy-loss (in ITS and TPC) and time-of-flight measurements (in TOF) [21].

- **Transition Radiation Detector** (TRD) : provides electron identification in the central barrel for momenta above 1 GeV/c. This is acheived by the conjunction with the TPC and the ITS through energy loss in pp and Pb-Pb collision. In this way, the reconstruction of the charm and beauty signal in the semi-leptonic decay channel is possible [22].

- **PHOton spectrometer** (PHOS) : it is an electromagnetic calorimeter with high resolution. Its role is to measure photons that gives information on the temperature of the system in the initial phase of the collision. The PHOS is made of lead-tungstate crystal ($PbWO_4$) which is dense and transparent.

- **ElectroMagnetic Calorimeter** (EMCal): is a large Pb-scintillator sampling calorimeter with cylindrical geometry adjacent to the ALICE magnet. EMCal enables ALICE to explore in detail the physics of jet quenching (interaction of energetic partons with dense matter) over the large energy accessible at the LHC. It covers $|\eta| \leq 0.7$ and its size is limited by the free space and the maximum weight that the L3 magnet can support [16].

- **Zero Degree Calorimeters** (ZDC): measures the remnant of the colliding nuclei (protons and neutrons which do not participate in the collision). It is located at 110 m on both sides of the interaction point along the beam axis [23].

- **T0** : it consists of two arrays of Cherenkov counters (12 counters per array) that are located on both sides of the interaction point (IP). Its role is to measure with high precision the time at which the event takes place for the TOF detector. T0 covers a pseudorapidity range $-3.3 < \eta < -2.9$ and $4.5 < \eta < 5$.

- **Forward Multiplicity Detector** (FMD): Its role is to measure charged particles produced in the collision in the pseudorapidity range $-3.4 < \eta < -1.7$ and $1.7 < \eta < 5.0$. The FMD consists of silicon strip channels distributed over 5 ring

counters. It provides information on charged particle multiplicity for all collision systems. The FMD is limited in space by the presence of the ITS, TPC and muon arm whose dimensions were decided before those of the FMD.

- **V0** : consists of 2 disks of segmented plastic scintillator tiles (named V0A and V0C) located on both sides of the ALICE collision vertex. It is a small-angle detector with a pseudorapidity coverage similar to the FMD. The principle function of the V0 detector is to trigger the data taking and determine the centrality of the event [24].

In general smaller detectors (ZDC, PMD, FMD, T0, V0) are for global event characterization and triggering the reason for which they are located at small angles [16, 17, 25].

2.2.2 Forward Muon spectrometer

The second principle part of the ALICE detector is the forward muon spectrometer. It covers a pseudorapidity range of $-4.0 < \eta < -2.5$. The elements that constitute the muon spectrometer are the dipole magnet, ten planes of trackers and two trigger chambers and absorbers (front absorber, iron wall, beam shield, rear absorber).

The muon spectrometer measures heavy flavours, quarkonia and light resonances through their decay into muons and dimuons. So, it is necessary to detail each element of its constituants and the role of each one [16, 17, 25, 26].

Figure.2.3 contains a layout of the forward muon spectrometer with its different parts:

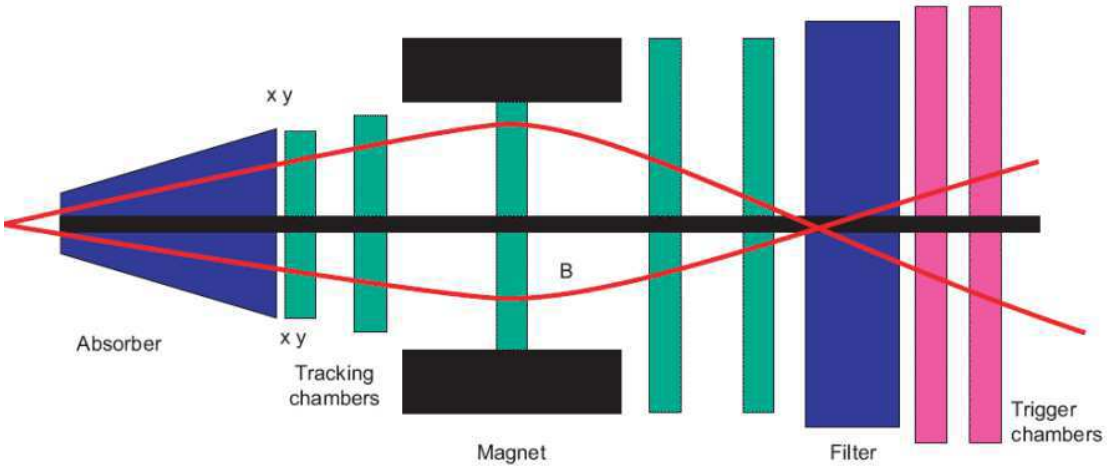

FIGURE 2.3: The forward Muon spectrometer layout of main components. An absorber to filter the background, a set of tracking chambers before, inside and after the magnet and a set of trigger chambers.

2.2.3 Absorbers

A front absorber is located inside the solenoid magnet and it is 4.13 m length. It is made of carbon and concrete to limit small-angle scattering and energy-loss by traversing muons. The spectrometer is shielded throughout its length by a dense absorber tube surrounding the beam pipe. It has a conical geometry to reduce background particle interaction along the length of the spectrometer. While the front absorber and the beam shield are sufficient to protect the tracking chambers, additional protection is needed for the trigger chambers. For this reason the muon filter, i.e. an iron wall 1.2 m thick ($\sim$ 7.2 λ_{int}), is placed after the last tracking chamber, in front of the first trigger chamber. The front absorber and muon filter stop muons with momentum less than 4 GeV/c.

2.2.4 Tracking system

The tracking system consists of 5 stations each containing two chambers. Each chamber is below 3% radiation length in terms of thickness. They are made of composite material to minimize the scattering of the muons so that required resolution is obtained. The 5 stations are based on standard multiwire proportional chambers for which the imposed constraints are different:

- **Stations 1 and 2** cover the smallest surface area in the forward cone and only high particle densities (up to 4 $\times 10^{-2}$ hits/cm^2 for station 1) are observed. The two stations are placed before of the muon magnet at a distance of $\sim$ 5.4 m and $\sim$ 6.8 m respectively from the IP.

- For **station 3**, lower particle flux (below 6×10^{-3} hits/cm^2) is seen but that station is located inside the dipole magnet and that helps to minimize the effects of multiple scattering so that resolution on mass is preserved.

- For **stations 4 and 5**, they are in the intermediate situation in terms of particle fluxes and they have very large surface areas.

Stations 3, 4 and 5 are placed at a distance of $\sim$ 9.7 m (inside the muon magnet), $\sim$ 12.65 m and $\sim$ 14.25 m from the IP. The transverse momentum is determined from the parameter characterizing the bending plane ($|p_{zy}|$) after the particles are influenced by the magnetic field in the third station.

2.2.5 Trigger system

The trigger system is designed to impose selection on tracks and events that will be used later for analysis. The trigger system consists of 4 planes of Resistive Plate Chambers that are assembled in 2 stations and located after the passive muon filter. Since there is important background at low p_t, there is a cut imposed on the transverse momentum of the tracks to reduce background. The two stations are located at about 16 m from the interaction point and 1 m apart.

2.2.6 Dipole magnet

The dipole magnet is one of the biggest warm dipoles in the world. The overall dimensions of the magnet are 5 m in length, 6.6 m wide, and 8.6 m high. The weight of the magnet is about 800 t. It is located at 7 m of the interaction point. It is characterized by a magnetic field of B = 3 Tm field integral. The dipole magnet is also a support for the muon front absorber and the beam shield.

Chapter 3

Background subtraction

The present analysis is performed using the 2011 proton-proton collisions at 7 TeV registred by the ALICE experiment. The p_t-shape of the background is extracted using realistic simulations of proton-proton collisions at 7 TeV from 2010 (those of 2011 are not yet available). The simulations will be introduced with two models of event generators (PYTHIA and PhoJet). And then, the systematic uncertainties are estimated on each step of the subtraction procedure.

3.1 Realistic simulations

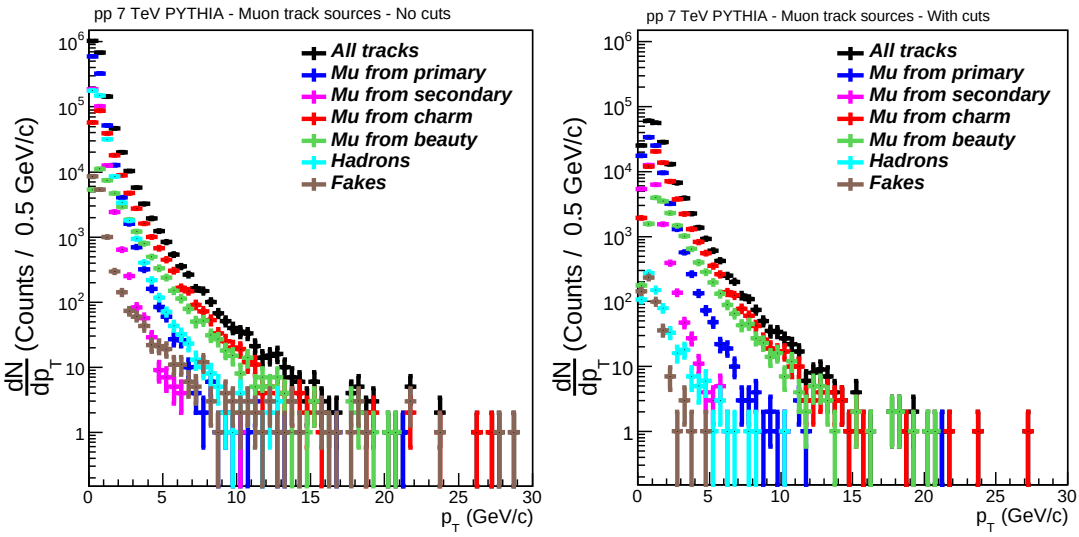

FIGURE 3.1: Transverse momentum ditributions of muon track sources in pp collisions at $\sqrt{s} = 7$ TeV obtained from simulations with PYTHIA, without (left) and with (right) event and track selection.

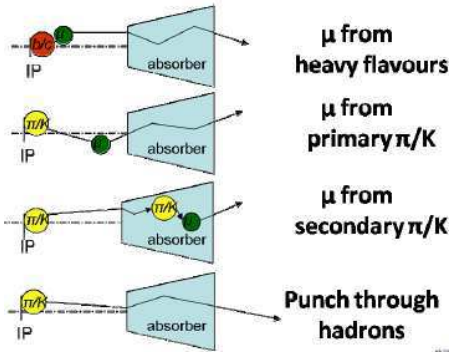

FIGURE 3.2: The production mechanisms for different muon track sources.

Realistic simulations (figure.3.1) show that muons detected in the muon spectrometer are coming from different sources. The left panel of figure.3.1 shows the p_t-spectrum of muon tracks reconstructed in the muon spectrometer without any selection cuts.

There are muons from Open Heavy Flavour decay (charm and beauty). They have short lifetime and they decay directly after their production into single muons as it is shown in figure 3.2.

Muons from light hadrons decay which primary K/π are the most dominant (as it is shown in appendix.A). The production of those muons depends on the distance travelled by kaons and pions after their production in pp collision before reaching the front absorber.

But not all light hadrons decay into muons before the front absorber. Actually, some of them reach the front absorber and interact with it to produce muons. The production of these secondary muons depends on the interaction probability with the front absorber.

In the spectrum, there are also hadrons which were misidentified as muons and fake tracks resulting from the noise of the detector. The inclusive muon spectrum is also shown in the same figure and it represents muons from all muon sources.

The p_t-spectrum of muons from realistic simulation that will be used is the one obtained after applying the selection cuts (see right panel of figure.3.1).

The selected events have at least one reconstructed interaction vertex. Various track cuts were applied in order to further reduce the background contributions in the data sample.

- Tracks were required to be reconstructed in the geometrical acceptance of the muon spectrometer, with $-4.0 < \eta < -2.5$ and $171^\circ < \theta_{abs} < 178^\circ$, θ_{abs} being the track polar angle measured at the end of the absorber.

- Then, the track candidate measured in the muon tracking chambers was required to be matched with the corresponding one measured in the trigger chambers. This results in a very effective rejection of the hadronic component that is absorbed in the iron wall.
- The correlation between momentum and Distance of Closest Approach (DCA, distance between the extrapolated muon track and the interaction vertex, in the plane perpendicular to the beam direction and containing the vertex) was used to remove remaining beam-induced background tracks which do not point to the interaction vertex. Indeed, due to the multiple scattering in the front absorber, the DCA ditribution of tracks coming from the interaction vertex is expected to be described by a Gaussian function whose width depends on the absorber material and is proportional to $1/p$. The beam-induced background does not follow this trend and can be rejected by applying a cut on $p\times$ DCA at 5 σ. The width is extracted from a Gaussian fit to the p $\times$ DCA distribution measured in two regions in θ_{abs}, corresponding to different materials in the front absorber.

By comparing the spectra with and without selection cuts, one can notice that all fake tracks are suppressed for $p_t > 5$ GeV/c, hadrons also are suppressed for $p_t \gtrsim 10$ GeV/c. So hadrons and fake tracks are reduced partially after applying selection cuts. The main background source is the primary muons while the amount of secondaries, hadrons and fakes are negligible.

3.2 p_T-shape of the background

In our study, we will focus on the range of $p_t > 2$ GeV/c, because the dominant background which is muons coming from primary K/π is dominant in the range $0 < p_t < 2$ GeV/c, with respect to the signal in interest which is muons from heavy flavours.

The background which will be subtracted is the muons from primaries. Its p_T-shape had to be extracted from realistic simulation using the same selection cuts applied on the real data. Then, the obtained p_t-shape of background is normalized to the real data to estimate the background. After subtracting the background, we are left with the spectrum of muons from open heavy flavour.

To obtain p_t-shape, spectrum of primary muons is fitted using the function defined by the equation.3.1

$$f(p_T) = \frac{A}{(B^2 + p_t^2)^n} \tag{3.1}$$

where A, B and n are free parameters.

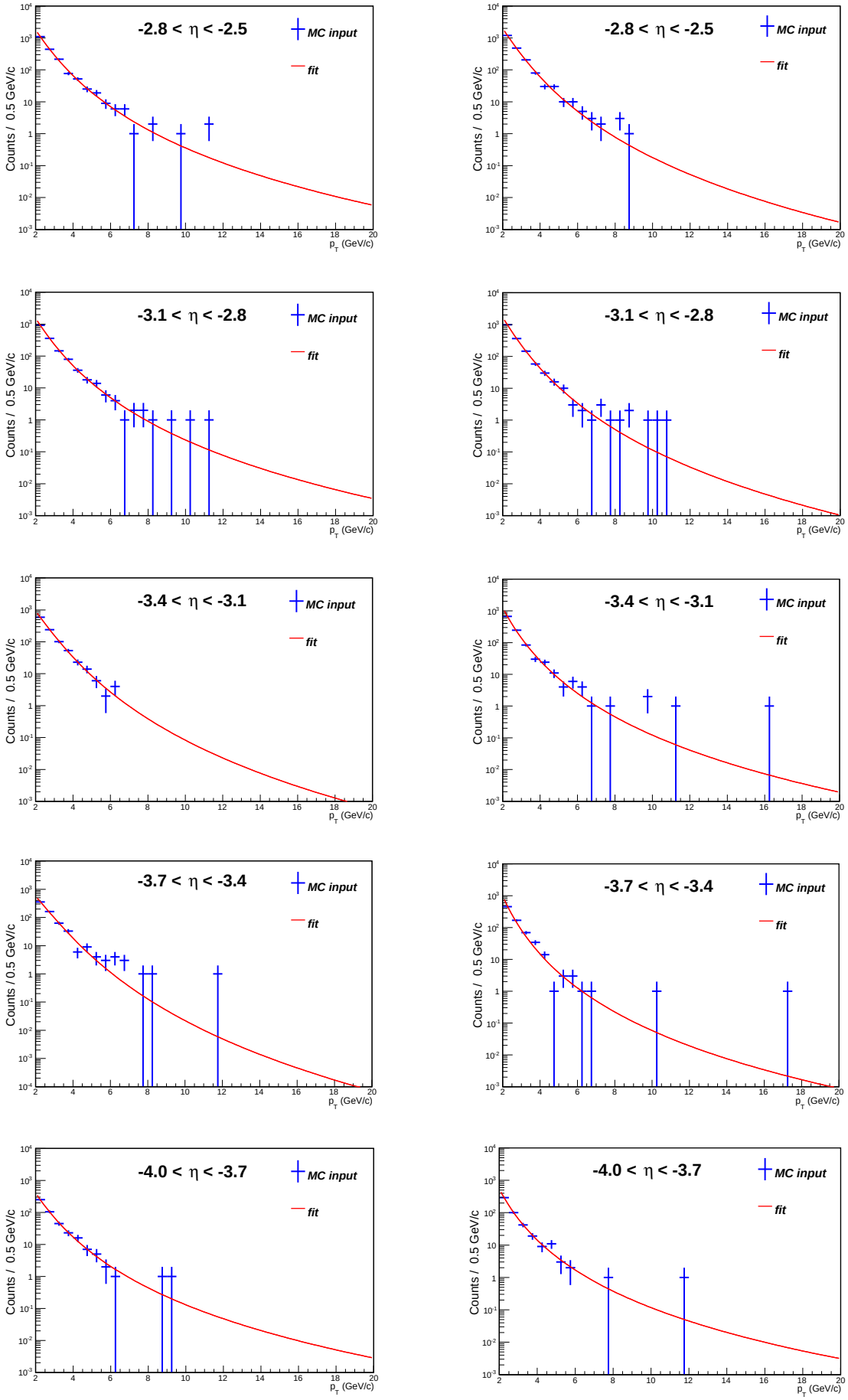

FIGURE 3.3: Fit and extrapolation of the primary muons p_t-spectrum in the 5η bins using PYTHIA (left) and PhoJet (right).

But this is not sufficient since primary muons spectrum is up to 12 GeV/c (after selection cuts, statistics of primary muons are not large enough) while that of inclusive muons from real data is up to 20 GeV/c. An extrapolation up to 20 GeV/c is required using the same previous function for fit. The fit and extrapolation in each η bin is shown in figure.3.3.

The procedure of fitting and extrapolation at high p_t may influence the results introducing additional systematic uncertainties on background estimation. For that reason and before going ahead the validation of the stability of the procedure should be done.

We perform the following cross-check for both PYTHIA and PhoJet :

1. We divide the total acceptance in pseudorapidity ($-4.0 < \eta < -2.5$) into 5 equally sized bins.
2. Fit the primary muons p_t-spectrum from 2 to 20 GeV/c in each pseudorapidity bin and sum over the 5 bins to get the p_t-spectrum of primary muons in the total η region.
3. Fit the p_t-spectrum of primary muons in the total acceptance.
4. Compare results from steps 2 and 3.

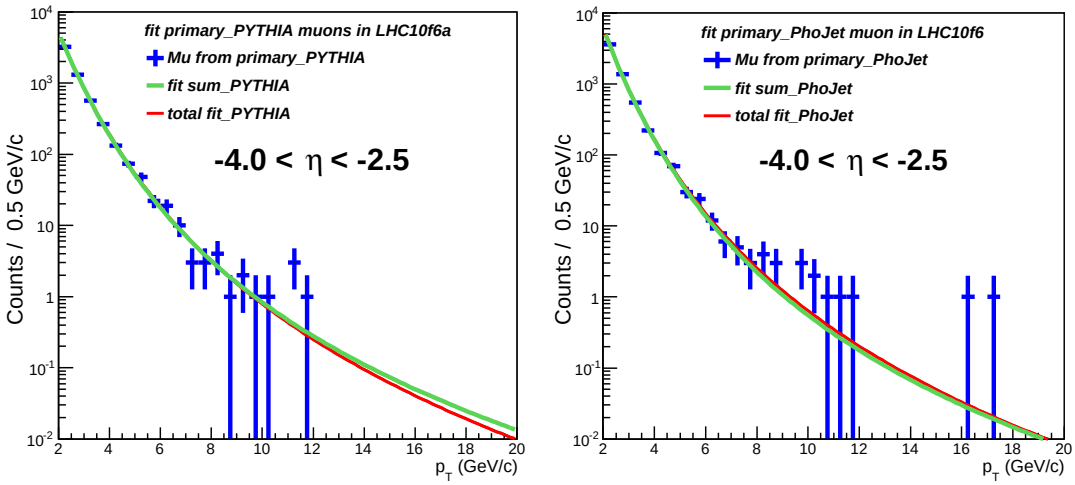

FIGURE 3.4: Comparison between the p_T-shape of primary muons in the total acceptance $-4.0 < \eta < -2.5$ (red line) and the sum from the fit in the 5 pseudo-rapidity bins (green lines). Left panel : PYTHIA. Right panel : PhoJet.

The comparisons of the resulting fits are shown in figure.3.4. The green curve is the sum of the fit from the 5 pseudo-rapidity bins individually and the red curve is the fit in the total acceptance. The comparison between both shows that they are compatible with each other, but there is a slight difference at high p_t for PYTHIA, which could be explained due to the fact that there is not enough statistics. In addition to that, the

background at high p_t-region is small with respect to the signal, so the signal is weakly affected by the background at high p_T. The strategy of fit and extrapolation to extract the p_T-shape of the background is then stable and the procedure is validated.

3.3 Background Normalization

The statistics in real data and in simulations are different. To perform the subtraction, p_t-shapes of the background from simulations should be scaled to real data. For this purpose, scaling factors (defined by the equation.3.2) are calculated to perform the normalization of spectrum from simulations. The background p_t-shape is then subtracted from the p_t-spectrum of real data.

$$S_{MC}(\Delta\eta) = R_{MC}(\Delta\eta) \times \frac{N_{RD}^{inclusive\mu}(lowp_t, \Delta\eta)}{N_{MC}^{primary\mu}(lowp_t, \Delta\eta)} \tag{3.2}$$

where the factor R_{MC} is the ratio between the yield of primary and inclusive muons in the same $\Delta\eta$ region and it is represented by the equation.3.3,

$$R_{MC}(\Delta\eta) = \frac{N_{MC}^{primary\mu}(lowp_t, \Delta\eta)}{N_{MC}^{inclusive\mu}(lowp_t, \Delta\eta)} = \frac{N_{RD}^{primary\mu}(lowp_t, \Delta\eta)}{N_{RD}^{inclusive\mu}(lowp_t, \Delta\eta)} \tag{3.3}$$

such that,

$$N_{RD/MC}^{inclusive\mu/primary\mu}(p_t, \Delta\eta) = \int_{\Delta\eta} \mathrm{d}\eta \int_0^{1GeV/c} \mathrm{d}p_t \frac{d^2N^{inclusive\mu/primary\mu}}{dp_t d\eta} \tag{3.4}$$

where N is the number of muon tracks (primary or inclusive) with $0 < p_t < 1$ GeV/c (where the background is dominant) in a given $\Delta\eta$ region from data or simulations.

Using the expression of R_{MC} and $S_{MC}(\Delta\eta)$ defined by the equation.3.3 and equation.3.2 respectively, the final expression of the scaling factors that were used for normalization is represented by the equation.3.5.

$$S_{MC}(\Delta\eta) = \frac{N_{RD}^{inclusive\mu}(lowp_t, \Delta\eta)}{N_{MC}^{inclusive\mu}(lowp_t, \Delta\eta)} \tag{3.5}$$

There is a scaling factor computed for each η-bin and for each model, to scale the p_t-spectrum extracted of primary muons in each $\Delta\eta$ region so that we could estimate the

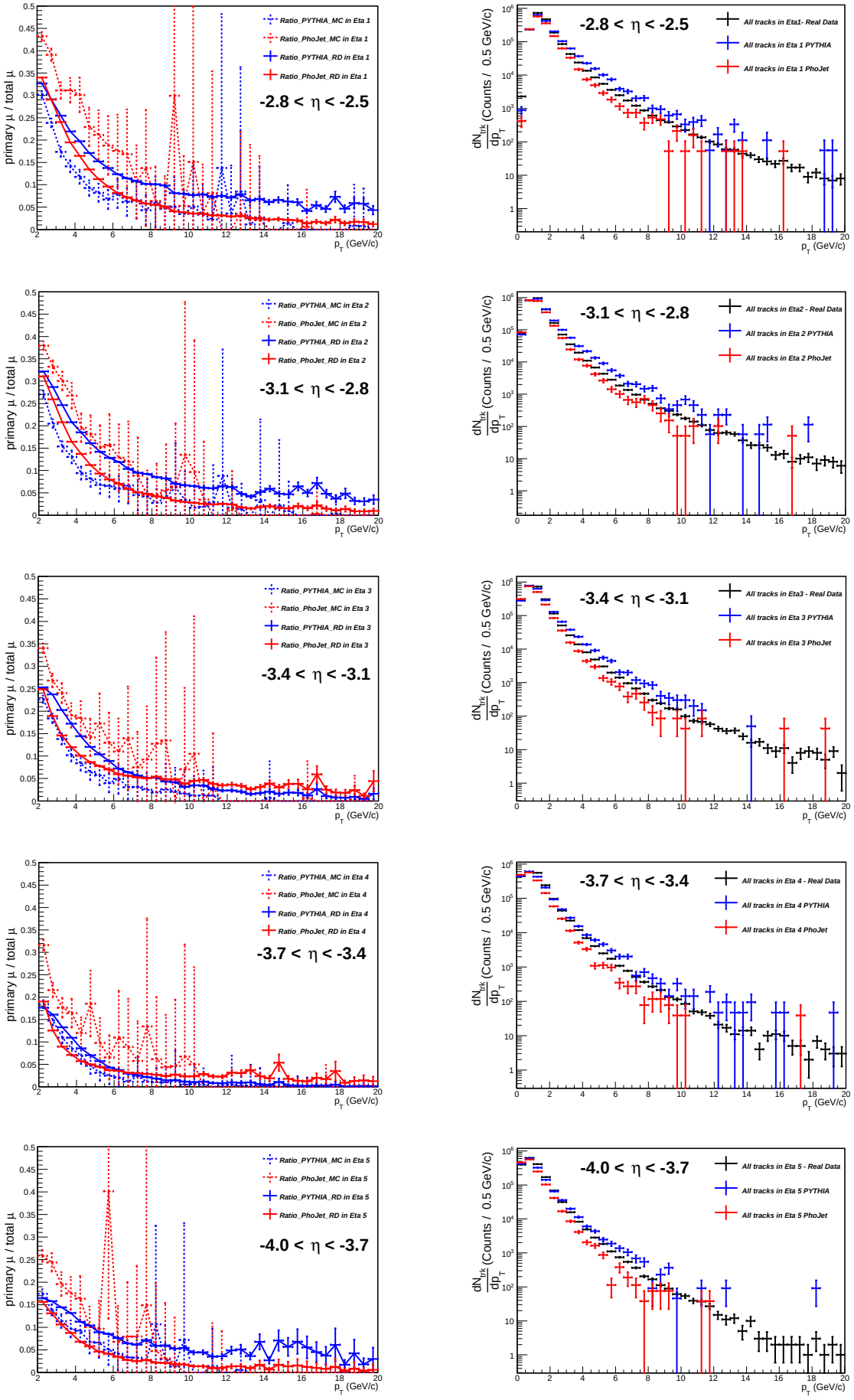

FIGURE 3.5: Estimated ratio of primaries (scaled) to inclusive muons for real data and Monte Carlo simulations (left) and comparison between the inclusive spectrums of real data and Monte Carlo simulations (right) in the 5 η bins.

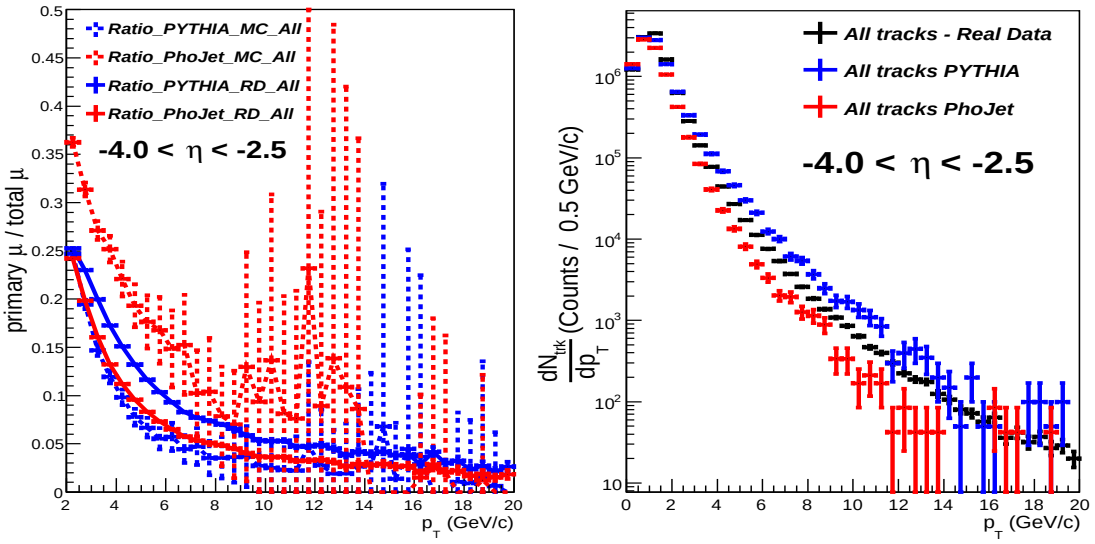

FIGURE 3.6: The same as figure.3.5 in $-4.0 < \eta < -2.5$.

yield of primary muons in real data. The scaling factors obtained for each η bin and for each model are presented in Appendix.B.

The left panel of figure.3.6 represents the ratios between primary and inclusive muons, this is, the estimated background in data and in simulations in the total acceptance. The primary muons spectrum is already scaled with $S_{MC}(\Delta\eta)$. It is noticed that the estimated background is decreasing with increasing p_t. That behaviour is the same more or less in the four curves. The background is important at low p_t approximately up to 25% for real data but at high p_t the background is small. It is possible to say that the signal is less sensitive to the background at high-p_t while at low p_T, the signal is much more contaminated with respect to high p_T.

The right panel of figure.3.6 represents the p_t spectrum of inclusive muons from real data and from simulation for different models. One can notice that the behaviour of p_t spectrum of muons is similar between real data and Monte Carlo simulation, there is only a difference in yield.

The p_t spectrum of muons from data and simulations and the estimated background in each η bin are also shown (see figure.3.5).

3.4 Results

After the calculation of the scaling factors and normalizing the primary muon spectrum to the real data, the ratio of primary muons (background) is estimated in real data and

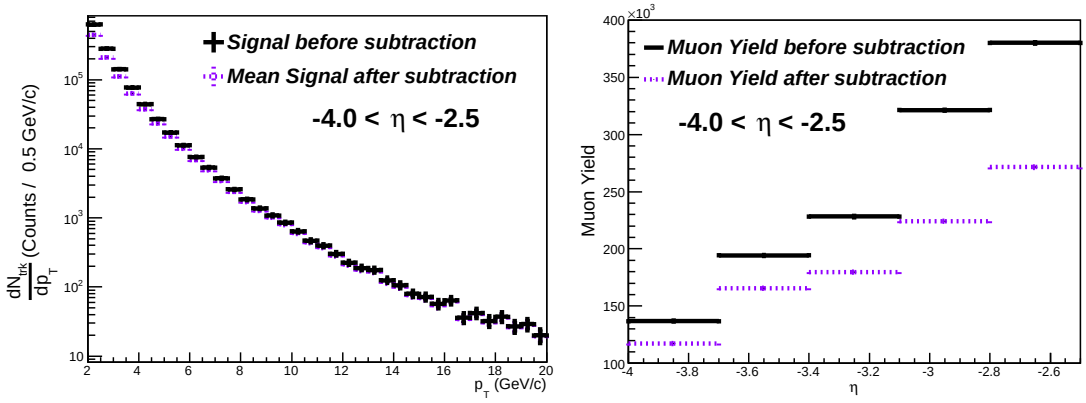

FIGURE 3.7: Left panel : yield of muons before background subtraction and the mean yield after the background subtraction from PYTHIA and PhoJet as a function of p_T in $-4.0 < \eta < -2.5$. Right panel : yield of muons before and after background subtraction as a function of η and for $2 < p_T < 20$ GeV.

in simulations. The subtraction of the background is performed and we obtain the p_T-spectrum of muons from heavy flavour decay (see left panel of figure.3.7) and the η-yield of muons from open heavy flavour decay (right panel of figure.3.7). The final signal is the average coming from the two signals obtained using the two estimated primary muon spectrum from different simulation models.

3.5 Systematic uncertainties

Systematic uncertainties arise from different steps in the procedure followed to subtract the background. First, we have fitted and extrapolated the p_t-spectrum of the primary muons from realistic simulations and from that procedure we can ignore the systematic uncertainties. The following step was the subtraction where two background shapes were used, then there is an uncertainty due to the different models σ_{model}. Next, the p_t-shapes of the background were normalized to real data. The normalization is influenced by the different transport processes that introduce an other kind of uncertainties (σ_{norm}).

We begin by σ_{model} which is simple to find. The signal is obtained after subtraction using the two models. The mean value of the two previous signals is computed in the total acceptance and in each η-bin separately. The average gives the central value of the muons signal and σ_{model} is given by the ratio between the average spectrum and the two signals obtained after background subtraction using PYTHIA and PhoJet. The ratio is shown in the left panel of figures.3.8 in the 5 η bins. This systematic uncertainty is relatively small and we can consider that it does not depend on p_t, but only on the η bin. For this reason, σ_{model} is taken to be the maximum deviation in each η bin.

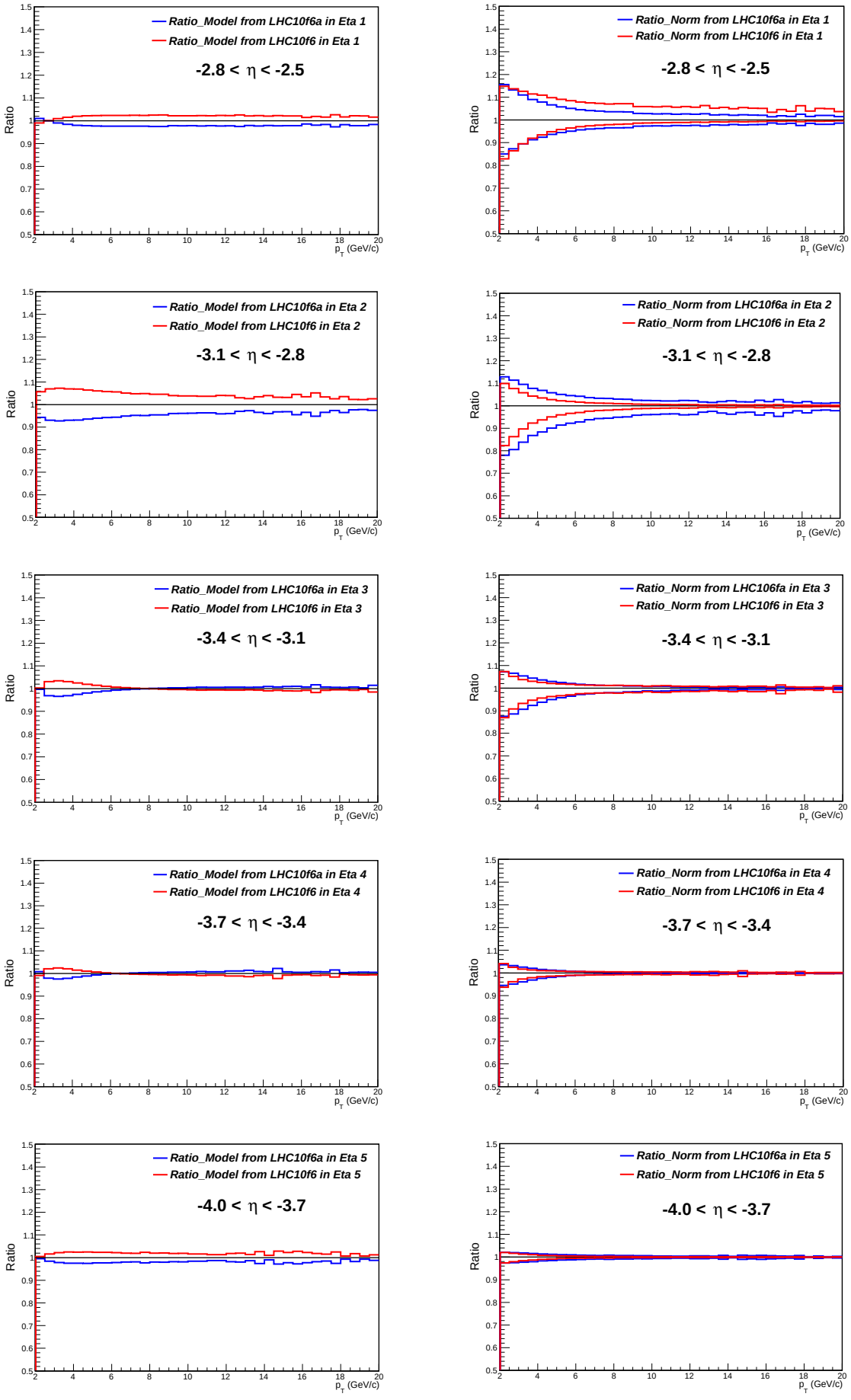

FIGURE 3.8: Estimated systematic uncertainties for σ_{model} (left) and σ_{norm} (right) in the 5 η bins.

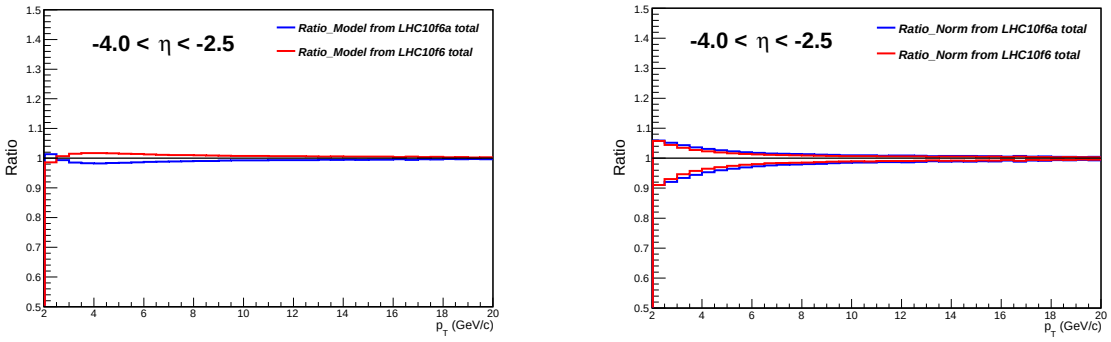

FIGURE 3.9: Estimated systematic uncertainties for σ_{model} (left) and σ_{norm} (right) in the total acceptance.

For σ_{norm}, it is not straightforward. The uncertainty is due to normalization. The transport codes (GEANT3 and Fluka) used in Monte Carlo simulations do not give the same yield of secondary muons that are produced inside the front absorber. It is assumed that the difference in secondary yield between the transport processes is 100% which means that two cases are considered : no secondary muons or two times more secondary muons. The variation of the secondary yields influences inclusive muon yields and as a consequence the normalization will be different. So, new scaling factors had to be calculated (see Appendix.B). The systematic uncertainty is given by the ratio between the spectrum with the new scaling factors and the original one for each model and for each η bin.

According to the right panel of figure.3.8, σ_{norm} does not depend on η bin only but also on each p_t value. One can also notice that σ_{norm} is not small as in σ_{model}.

Results on systematic uncertainties are shown in figure.3.8 and the corresponding values of uncertainties are introduced in table.3.1.

Systematic uncertaities in the total η region were also calculated and presented in table.3.1. The associated ratios are shown in figure.3.9.

TABLE 3.1: Estimated systematic uncertainties for σ_{model} and σ_{norm}.

	σ_{model}	σ_{norm}															
		p_t (GeV/c)															
		2-2.5	2.5-3	3-3.5	3.5-4	4-4.5	4.5-5	5-5.5	5.5-6	6-6.5	6.5-7	7-7.5	7.5-8	8-8.5	8.5-9	9-9.5	10-20
$2.5 < \eta < 4.0$	2%	9%	8%	7%	6%	5%	4%	3.5%	3%	$< 3\%$							
$2.5 < \eta < 2.8$	3%	17%	14%	13%	12%	11%	10%	9%	8.5%	8%	7.5%	7%	7%	7%	7%	6%	$< 6\%$
$2.8 < \eta < 3.1$	7%	22%	19.5%	16%	13%	12%	10%	9%	8%	7%	6%	6%	5.5%	5%	5%	4%	$< 4\%$
$3.1 < \eta < 3.4$	3.5%	13%	12%	9.5%	8%	6%	5%	4%	$< 4\%$								
$3.4 < \eta < 3.7$	2.5%	6%	5%	4%	$< 4\%$												
$3.7 < \eta < 4.0$	2.5%	3%															

Chapter 4

Conclusion

Heavy flavours are produced in the early stages of heavy ion collisions making them good probes for the Quark Gluon Plasma. In proton-proton collisions, heavy flavours can also be used to test perturbative QCD calculations. In addition to that, their study is of great importance because they are a natural normalization in the study of heavy ion collisions.

The ALICE experiment studies quarkonia and open heavy flavour at mid and forward rapidity. The muon spectrometer measures single muons from open heavy flavour decay and dimuons from quarkonia decay in a pseudorapidity coverage of $-4.0 < \eta < -2.5$.

The p_t spectrum of inclusive muons detected with the muon spectrometer contains different muon sources. In order to subtract the background, muons from light hadron decays, the p_t-shape was determined using realistic simulations with different event generators using fit and extrapolation strategy. The subtraction was performed in the range $2 < p_t < 20$ GeV/c since the background is dominant in the range [0,2] GeV/c. The resulting p_t spectrum was scaled to real data to estimate the background. Then, the background was subtracted using two diffrent models to obtain the final signal of open heavy flavour given by the average of the two signals obtained after background subtraction. Systematic uncertainties were estimated on each step of the subtraction procedure. The uncertainties on the fit and extrapolation has been assumed to be negligible. Uncertainties from models were found to be small and η dependent. Uncertainties from normalization were found to be important and depend on both p_t and η.

Appendix A

π/K Dominant Primary particles

In the present appendix, we are presenting in tables from A.1 to A.6, the main sources of muons coming from light hadron decay, charm and beauty hadrons decay.

Two event generators were used. For each, rounded percentages of each particle that contributes in the muon spectrum are presented in these tables. Such an example, table.A.1 and table.A.4 are presenting the percentages of light hadrons that have decayed into muons from PYTHIA and PhoJet. From table.A.1, one can notice that the percentage of Kaons and pions together is approximately 63%. Then, dominant primary particles decaying into muons are pions and kaons.

Rounded percentages for muons coming from charm and beauty particles can be found in table.A.2 and table.A.3.

The percentage of primaries and open heavy flavours could be extracted from simulations using PhoJet also. The rounded values are presented in table.A.4 for light hadrons and table.A.6 for beauty particles and table.A.5 for charm particles.

TABLE A.1: Produced primary particles according to PYTHIA

Muons from primary		
PDG code	Particle	Pourcentage
211	π^+	33 %
321	K^+	22 %
113	$\rho^0(770)$	11 %
213	$\rho^0(770)$	10 %
313	$K^{*0}(892)$	8 %

Table A.2: Produced open charm particles according to PYTHIA

Muons from Charm		
PDG code	Particle	Pourcentage
411	D^+	37 %
413	$D^{*+}(2010)$	24 %
423	$D^{*0}(2007)$	16 %
421	D^0	14 %
433	D_s^{*+}	3 %

Table A.3: Produced open beauty particles according to PYTHIA

Muons from Beauty		
PDG code	Particle	Pourcentage
513	B^{*0}	25 %
511	B^0	21 %
523	B^{*+}	22 %
521	B^+	19 %
533	B_s^{*0}	4 %

Table A.4: Produced primary particles according to PhoJet

Muons from primary		
PDG code	Particle	Pourcentage
211	π^+	28 %
213	$\rho^+(770)$	11 %
113	$\rho^0(770)$	12 %
313	$K^{*0}(892)$	13 %
321	K^+	16 %
323	$K^{*+}(892)$	8 %

Table A.5: Produced open charm particles according to PhoJet

Muons from Charm		
PDG code	Particle	Pourcentage
421	D^0	49 %
411	D^+	42 %
431	D_s^+	8 %

TABLE A.6: Produced open beauty particles according to PhoJet

Muons from Beauty		
PDG code	Particle	Pourcentage
511	B^0	46 %
521	B^+	44 %
531	B_s^0	7 %

Appendix B

Scaling factors

In this appendix, values of the scaling factors are given for the 5 η bins and for the total η region for each simulation model. Those values are used to scale the p_t-shape of the background (primary muons) to real data.

The final expression to compute the scaling factors is defined by the equation.3.5 assuming that the expression is valid only at low p_t ($p_t < 1$ GeV/c) where the background is dominant.

The obtained rounded values are summarized in table.B.1.

We also show the scaling factors used to determine the systematic uncertainties in the case of σ_{norm}. Indeed, as mentioned in chapter 3, the number of muons coming from

TABLE B.1: Scaling factors (rounded) used to scale the background to the real data

pseudorapidity	Scaling factor	
	PYTHIA	PhoJet
$-4.0 < \eta < -2.5$	50	42
$-2.8 < \eta < -2.5$	56	53
$-3.1 < \eta < -2.8$	57	51
$-3.4 < \eta < -3.1$	50	42
$-3.7 < \eta < -3.4$	47	39
$-4.0 < \eta < -3.7$	46	38

TABLE B.2: Scaling factors used for background subtraction and to compute σ_{norm}.

Pseudorapidity	Scaling factor					
	PYTHIA			PhoJet		
	2* secondary muons	original	0* secondary muons	2* secondary muons	original	0* secondary muons
$-4.0 < \eta < -2.5$	41	50	63	35	42	54
$-2.8 < \eta < -2.5$	45	56	73	42	53	70
$-3.1 < \eta < -2.8$	45	57	77	40	51	71
$-3.4 < \eta < -3.1$	39	50	68	33	42	59
$-3.7 < \eta < -3.4$	39	47	57	32	39	49
$-4.0 < \eta < -3.7$	41	46	52	34	38	43

secondary particles depends on the transport of particles through the material. So σ_{norm} takes into account this dependence by varying, within 100%, the amount of secondary muons extracted with the different event generators. This leads to the fact that the inclusive number of muons would be changed and consequently the scaling factors. It means that there are two cases to consider when calculating the new scaling factors. One case is to consider that there is no secondary muons and the second case is that there are two times more secondary muons.

Bibliography

[1] Diego Stocco. *Development of the ALICE Muon Spectrometer: preparation for data taking and heavy flavor measurement.* PhD thesis, Università degli Studi di Torino, 2008.

[2] Francesco Prino. Open heavy flavour reconstruction in the alice central barrel. *ICHEP08, arXiv:0810.3086*, 2008.

[3] Francois Gelis. Some aspects of ultra-relativistic heavy ion collisions. *Acta Phys.Polon.Supp.*, 1:395–402, 2008.

[4] M. A. Stephanov. Non-gaussian fluctuations near the qcd critical points. *Phys. Rev. Lett.*, 102:0323301, Jan 2009.

[5] A. Andronic, F. Beutler, P. Braun-Munzinger, K. Redlich, and J. Stachel. Statistical hadronization of heavy flavor quarks in elementary collisions: Successes and failures. *Phys.Lett.*, B678:350–354, 2009.

[6] Lizardo Valencia Palomo. *Inclusive J/ψ production measurement in Pb-Pb collisions at $\sqrt{s_{NN}} = 2.76TeV$ with the ALICE Muon Spectrometer.* PhD thesis, Paris-sud University & IPN, 2013.

[7] M. Lunardon. Open heavy flavour detection in ALICE. *Nucl.Phys.Proc.Suppl.*, 167: 25–28, 2007.

[8] A. Adare et al. Energy loss and flow of heavy quarks in au-au collisions at $\sqrt{s_{NN}}$ = 200 gev. *Phys.Rev.Lett*, 98:172301, 2007.

[9] Serhiy Senyukov. Open heavy flavour analysis with the alice experiment at lhc,arxiv:1304.2189v1. *Phys.Lett.*, 2013.

[10] A Dainese. Measurement of heavy-flavour production in proton-proton collisions at $\sqrt{s} = 7$ tev with alice. *arXiv:1012.4036*, 2010.

[11] Betty Abelev et al. Heavy flavour decay muon production at forward rapidity in proton-proton collisions at $\sqrt{s} = 7$ tev. *Phys.Lett.*, B708:265–275, 2012.

[12] Xiaoming Zhang. *Study of Heavy Flavours from Muons Measured with the ALICE Detector in Proton–Proton and Heavy-Ion Collisions at the CERN-LHC*. PhD thesis, CENTRAL CHINA NORMAL UNIVERSITY and BLAISE PASCAL UNIVERSITY, 2012.

[13] Philip Bryant for the ALICE Collaboration Lyndon Evans. The cern large hadron collider: Accelerator and experiments, lhc machine. *Journal of Instrumentation*, 3: 158, 2008.

[14] 2014. URL http://home.web.cern.ch/topics/large-hadron-collider.

[15] 2014. URL http://home.web.cern.ch/about/experiments.

[16] ALICE Collaboration. The cern large hadron collider: Accelerator and experiment, the alice experiment at the cern lhc. *Journal of Instrumentation*, 3:245, 2008.

[17] 2008. URL http://aliceinfo.cern.ch/Public/en/Chapter2/Chap2_dim_spec.html.

[18] ALICE Collaboration. Alice, technical design report of the inner tracking system (its). *ALICE-DOC-2005-002 v.1*, 2003.

[19] ALICE Collaboration. Alice, technical design report of the time projection chamber. *ALICE-DOC-2003-011*, 2003.

[20] ALICE Collaboration. Alice, addendum to the technical design report of the time of flight system (tof). *ALICE-DOC-2004-002 v.1*, 2004.

[21] ALICE Collaboration. Alice, technical design report of the high momentum particle identification detector. *ALICE-DOC-1998-01 v.1*, 2001.

[22] ALICE Collaboration. Alice, technical design report of the transition radiation detector. *ALICE-DOC-2004-009 v.1*, 2004.

[23] ALICE Collaboration. Alice, technical design report of the zero degree calorimeter (zdc). *ALICE-DOC-2004-003 v.1*, 1999.

[24] ALICE Collaboration. Alice, technical design report on forward detectors: Fmd, t0 and v0. *ALICE-DOC-2004-010 v.1*, 2004.

[25] ALICE Collaboration. Alice, technical design report of the dimuon forward spectrometer. *ALICE-DOC-2004-004 v.1*, 2004.

[26] Gines Martinez. Physics of the muon spectrometer of the ALICE experiment. *J.Phys.Conf.Ser.*, 50:361–370, 2006.